Taylor & Francis
Taylor & Francis Group

Mapping spatial variations of iron oxide by-product minerals from EO-1 Hyperion

Jamshid Farifteh[a]*, Willem Nieuwenhuis[b], and Eduardo García-Meléndez[c]

[a]M3-Biores – Biosystems Department, Faculty of Bioscience Engineering, Katholieke Universiteit Leuven, Leuven, Belgium; [b]Faculty of Geo-Information and Earth Observation, University of Twente, Enschede, The Netherlands; [c]Area de Geodinamica Externa, Faculty of the Environmental Science, University of Leon, Leon, Spain

This study aimed to map mine waste piles and iron oxide by-product minerals from an Earth Observing 1 (EO-1) Hyperion data set that covers an abandoned mine in southwest Spain. This was achieved by a procedure involving data pre-processing, atmospheric calibration, data post-processing, and image classification.

In several steps, the noise and artefacts in the spectral and spatial domains of the EO-1 Hyperion data set were removed. These steps include the following: (1) angular shift, which was used to translate time sequential data into a spatial domain; (2) along-track de-striping to remove the vertical stripes from the data set; and (3) reducing the cross-track low-frequency spectral effect (smile). The Fast Line-of-sight Atmospheric Analysis of Spectral Hypercubes (FLAASH) algorithm in combination with the radiance transfer code MODTRAN4 was applied for quantification and removal of the atmospheric affect and retrieval of the surface reflectance. The data set was post-processed (filtering, spectral polishing) in order to remove the negative values and noise that were produced as the a result of de-striping and atmospheric calibration. The Mahalanobis distance algorithm is used to differentiate the area covered by mine piles from other main land-use classes. The spatial variations of iron oxide and carbonate minerals within the mine area were mapped using the Spectral Feature Fitting (SFF) algorithm.

The pre-processing of the data and atmospheric correction were vital and played a major role on the quality of the final output. The results indicate that the vertical stripes can be removed rather well by the local algorithm compared to the global method and that the FLAASH algorithm for atmospheric correction produces better results than the empirical line algorithm. The results also showed that the method developed for correcting angular shifts has the advantage of keeping the original pixel values since it does not require re-sampling.

The classification results showed that the mine waste deposits can be easily mapped using available standard algorithms such as Mahalanobis Distance. The results obtained from the SFF method suggest that there is an abundance of different minerals such as alunite, copiapite, ferrihydrite, goethite, jarosite, and gypsum within the mine area. From a total number of 754 pixels that cover the mine area, 43 pixels were classified as sulphide and carbonate minerals and 711 pixels remained unclassified, showing no abundance of any dominant mineral within the area presented by these pixels.

*Corresponding author. Email: farifteh@itc.nl

1. Introduction

Use of mineral resources through mining activities generates waste-rock piles and tailings, which are sources of environmental degradation in the case of mismanagement. The intensive mining of pyritic massive sulphide in the Iberian Pyrite Belt (IPB) in southwest Spain (Huelva province) since mid-nineteenth century (Galán et al. 2003) has generated large amounts of sulphide piles and tailings that have led to the formation of acidic and iron-rich water, severely contaminating soil and water in the region (Hudson-Edwards et al. 2003). Catastrophic events such as the breaching of the Aznalcóllar tailings dam in the Spanish Iberian pyrite belt raised significant environmental concerns and triggered considerable numbers of investigations aiming to assess the level of soil and water pollution and to develop cost–benefit methods for the monitoring of solid waste deposits and estimating potential environmental risks in terms of water and soil quality.

Previous studies suggest the presence of iron oxide by-product minerals and localized concentrations of potentially toxic elements in the mine areas of the Spanish Iberian pyrite belt (Alastuey et al. 1999; Pamo et al. 1999; Buckby et al. 2003). These minerals have different abilities to carry toxic trace elements and produce different amounts of acidic water (Velasco et al. 2005). Therefore, gathering information about sulphate minerals and their spatial distribution is vital for estimating the level of pollutants and defining the risk management strategies. One of the cost–benefit methods for monitoring mine waste deposits involves application of remote-sensing data and techniques. This is due to the well-known fact that remote-sensing data are widely available and relatively cheap compared to field measurements.

Spaceborne remote-sensing data have been widely used to obtain information regarding Earth surface properties due to their spatial and temporal availability. Hyperspectral imaging data with hundreds of spectral bands have been successfully used to monitor and map materials on the Earth surface (Goetz et al. 1985; Crowley 1993; Clark and Swayze 1995; Swayze et al. 2000; Farifteh et al. 2007). Consequently, a large variety of analysis methods have been developed, which currently are used as standard techniques for extraction of information from airborne and space-borne imageries. The new-generation spaceborne hyperspectral sensor, Earth Observing 1 (EO-1) Hyperion, provides high spectral resolution data, which recently have been used for mineral mapping and forest classification (Goodenough et al. 2003; Kruse, Boardman, and Huntington 2003).

The research aims to develop a cost–benefit method for mapping and monitoring the spatial variability of the mine waste sulphide deposits on the basis of their spectral characteristics. The main strategy is to employ a suitable and non-complex monitoring method that makes use of high-resolution spectral information obtained by spaceborne sensors and field measurements. The developed method should have the capabilities to discriminate areas covered by mine deposits and also provide quantitative information concerning the iron oxide by-product minerals formed at the surface and near the surface as a result of alteration processes. Furthermore, the developed method should have undemanding capabilities in terms of the data availability (especially field measurements) and implementation (simplicity), since it is expected to be used as a preliminary application tool. The objective of the study, as defined above, can be achieved by the procedure involving Hyperion data pre-processing, atmospheric calibration, data post-processing, image classification, data analysis, and validation results.

2. Study area

The study area (Las Herrerías mine area) is situated in southwest Spain between 37° 36′, 30″ to 37° 37′ 30″ N and 7° 16′ 10″ to 7° 18′ 30″ W (Figure 1). The mine is located in the
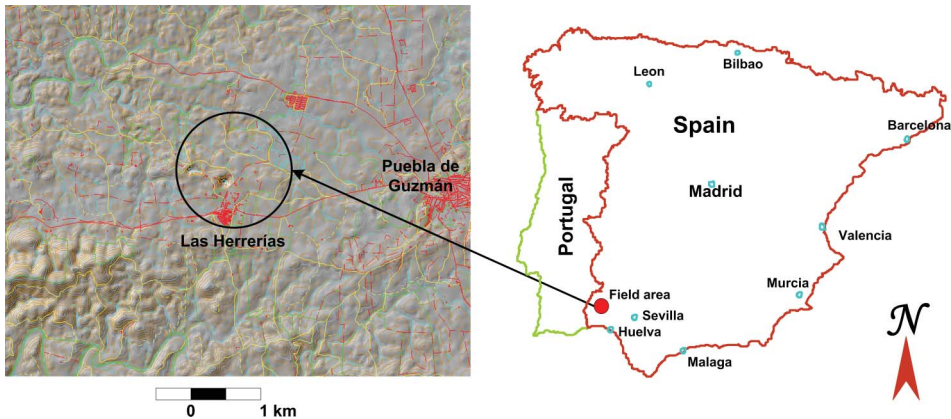
Figure 1. Location of the study area (Las Herrerías mine) in southwest Spain.

northwest of Huelva, at about 5 km from the village of Puebla de Guzmán and not very far from the Tharsis mine (15 km), which is one of the major mining districts in the area.

The Herrerías is a small- to medium-sized mine with a massive sulphide ore-body and a datable black shale formation, which can be associated with major massive sulphide deposits dated in the region (González et al. 2002; Sáez, Moreno, and González 2008). The sulphide ore-body consists mainly of pyrite, together with minor chalcopyrite, galena, sphalerite, arsenopyrite, and other accessory minerals (Doetsch 1957). The mining activities in the area, which date from Roman times, have been definitely ceased in Las Herrerías mining district since 1988 (Pinedo Vara 1963; Sáez, Moreno, and González 2008). Even though Las Herrerías, at the present time, is an abandoned mine, the large numbers of dumped waste-rock piles and tailings in the area are widely subjected to alteration processes (especially during summer due to high temperature), causing soil and water pollution. Recent studies suggest the presence of minerals such as haematite (Fe_2O_3), goethite ($FeO(OH)$), ferrihydrite ((Fe^{3+})$_2O_3 \cdot 0.5H_2O$), jarosite ($K(Fe^{3+})_3(SO_4)_2(OH)_6$), alunite ($KAl_3(SO_4)_2(OH)_6$), gypsum ($CaSO_4 \cdot 2H_2O$), epsomite ($MgSO_4 \cdot 7H_2O$), schwertmannite (($Fe^{3+}$)$_{16}O_{16}(OH)_{12}(SO_4)_2$), copiapite ($Fe^{2+}(Fe^{3+})_4(SO_4)_6(OH)_2 \cdot 20H_2O$), and localized concentrations of potentially toxic elements such as zinc (Zn), lead (Pb), arsenic (As), copper (Cu), cadmium (Cd), and chromium (Cr) in the area (Alastuey et al. 1999; Pamo et al. 1999). Figure 2 shows an overview and visual examples of the ongoing alteration process by which the waste-rock piles and tailings are weathered and various iron oxide by-product minerals are formed. These minerals potentially are a source of soil and water pollution by producing acid or iron-rich water during rainy seasons. A favourable geomorphologic setting, including an adequate drainage network in the area, increases the potential of the existing risk by facilitating mobilization of the produced acid water and toxic elements towards the downstream areas.

3. Materials

3.1. *EO-1 Hyperion data*

Hyperion is one of three sensors on board the EO-1 satellite launched in November 2000. The Hyperion push-broom instrument captures the incoming radiation in the visible and near-infrared (VNIR) and shortwave infrared (SWIR) wavelength range (400–2400 nm) in 242 spectral bands with an average full-width at half-maximum (FWHM) of 10.90 and
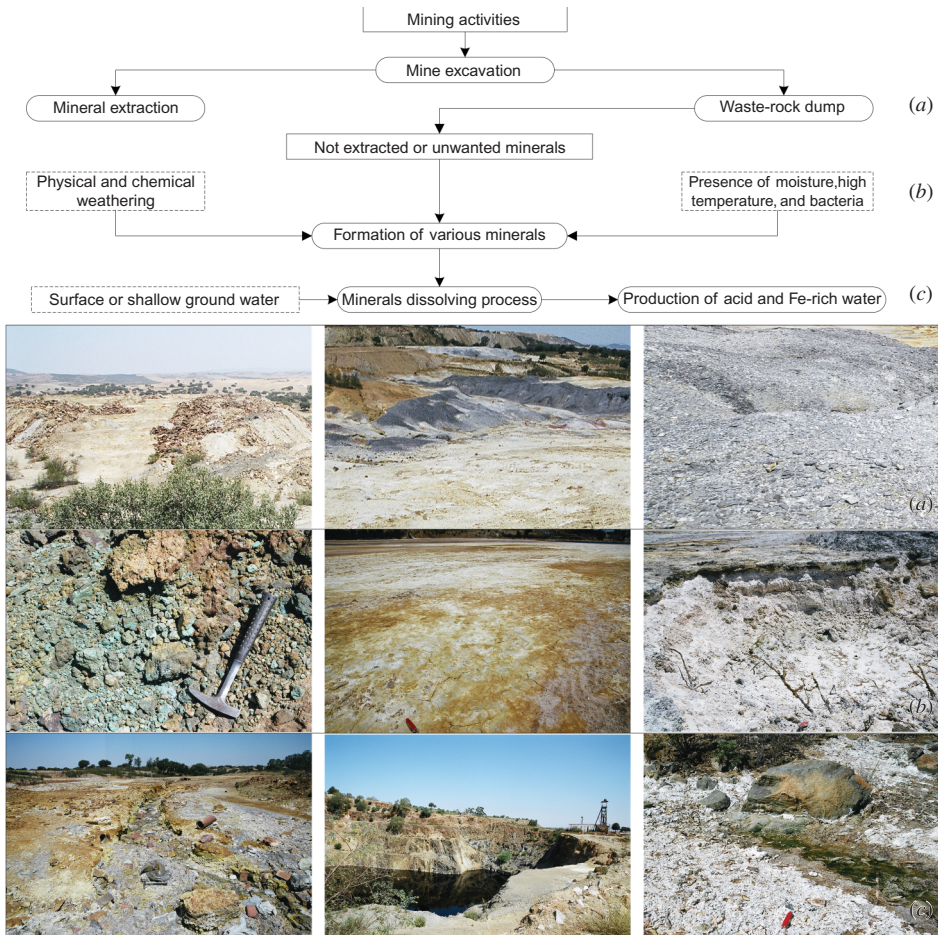
Figure 2. Flow chart of alteration processes (simplified); formation of iron oxide by-product minerals and acidic water. The photographs visualize the alteration process and the formation of various minerals and acidic water in the Las Herrerías mine area. (*a*) Examples of waste-rock piles and tailings, (*b*) formation of various minerals due to physical and chemical weathering, and (*c*) production of acid and iron-rich water due to dissolving of some of the minerals.

10.14 nm for VNIR and SWIR, respectively. It has 30 m spatial resolution with 7.65 km swath width from 705 km altitude. A detailed description of the Hyperion instrument and data are given in Barry (2001), Folkman et al. (2001), Pearlman et al. (2003), and Jupp and Datt (2006). The Hyperion data characteristics and their temporal availability provide a unique possibility (concerning the project objective) for mapping and monitoring main waste deposits in southwest Spain. However, the Hyperion level 1B1 data suffer from sensor artefacts and atmospheric effects (Datt et al. 2003; Goodenough et al. 2003), and therefore to optimize their application, it is essential that they are pre-processed and corrected prior to any data analysis.

In this study, the Hyperion level 1B1 data were used after they were converted to the BSQ format during which the pre-launched FWHM calibration setting was restored. From the available 242 bands, 196 bands (50 bands in VNIR and 146 bands in SWIR) cover the visible–near infrared–shortwave infrared (VNIR–SWIR) wavelength range between 426 and 2395 nm with no overlap with the NIR. They are bands 8–57 (426–925 nm) and

bands 79–223 (933–2395 nm). Among these 196 bands, 24 bands contain no information, which include bands 93–101 (1356–1437 nm), bands 138–152 (1810–1951 nm), and bands 195–196 (2385–2395 nm). There are also 25 bands that contain large amounts of noise including vertical or intermittent stripes. They are bands 1–3 (426–447 nm), bands 50–54 (925–962 nm), bands 69–72 (1114–1144 nm), bands 103–105 (1457–1477 nm), bands 153–158 (1961–2012 nm), and bands 191–194 (2345–2375 nm). These 25 bands can be used in data analysis after being de-striped and their signal-to noise ratio improved. In this study, after pre-processing and atmospheric correction of the EO-1 Hyperion data, only 166 bands are used to map the minerals and their spatial variations. They are bands 1–92 (426–1346 nm), bands 103–136 (1457–1790 nm), and bands 154–193 (1971–2365 nm). The Hyperion level 1B1 data were georeferenced by the United States Geological Survey (USGS).

3.2.   Field measurements

3.2.1.   Spectral measurements

A FieldSpec FR spectrometer, manufactured by Analytical Spectral Devices, Inc. (Boulder, CO, USA), was used to measure surface reflectance spectra of the rocks and soils within the study area. The instrument covers the visible to SWIR wavelength range using three separate detectors: one for VNIR (350–1050 nm) and two for the SWIR (1000–1800 nm and 1800−2500 nm). The spectrometer has a sampling interval of 1.4 nm for the region 350–1000 nm and 2 nm for the region 1000–2500 nm with a spectral resolution of 3 and 10 nm, respectively (ASD 2010).

Reflectance measurements were acquired in the 350–2500 nm range with a 25° field-of-view foreoptic from nadir at approximately 120 cm height above the surface between 11.00 am and 3:00 pm. Laboratory reflectance measurements were acquired in the aforementioned range and field-of-view from nadir at uniform 3 cm height above the approximately 2 cm thick soil and weathered rock samples. A light source, Lowel Light Pro, with a JCV 14.5 V–50 W halogen lamp, was used to illuminate the surface of the rock and soil samples from a 45° angle. Reflectance was calibrated using a white panel (Spectralon diffuse reflectance panel) in the field and the laboratory. The dark room used for the laboratory spectral measurements was painted with flat black paint to avoid spectral contamination.

4.   Methods

Analysis of the Hyperion data for mapping the types and spatial distributions of iron oxide minerals was carried out by developing approaches that allow reproducible results with minimum field and laboratory measurements. Implementation of the developed method was carried out using Environment for Visualizing Images (ENVI), interactive data language (IDL), and MatLab software. Figure 3 shows an overview of the developed methods, which includes data pre-processing, atmospheric correction, the mapping algorithm, and validation procedures.

4.1.   Pre-processing

The Hyperion level 1B1 data suffer from noise and sensor artefacts and have to be corrected prior to any data analysis (Staenz et al. 2002; Datt et al. 2003; Goodenough et al. 2003).
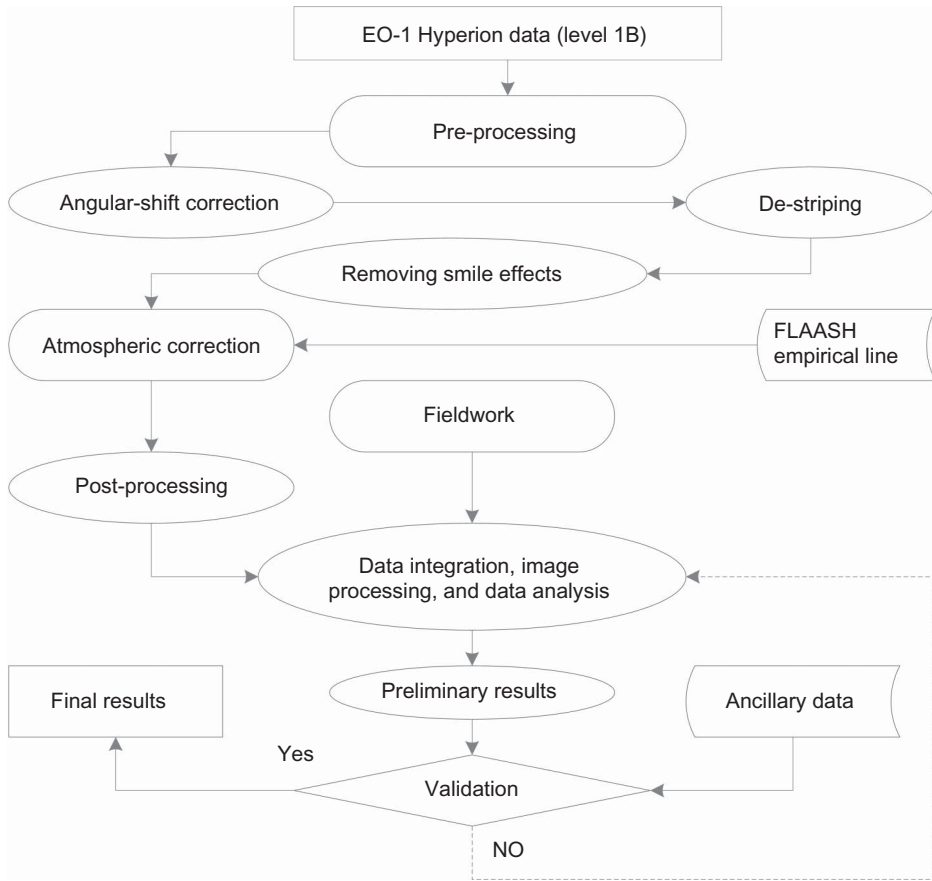
Figure 3. General methods for Hyperion data processing and mapping of iron oxide by-product minerals in the Las Herrerías mine district.

In this study, the Hyperion data were corrected for angular shift, vertical strips, and smile effects prior to atmospheric calibration (Figure 4).

4.1.1. *Angular-shift correction*

The angular shift occurs since the multiple detectors that are used to provide a wider spectral or spatial coverage become misaligned within the Hyperion instrument (Pearlman et al. 2003; White et al. 2004). As a result, the Hyperion data are not in the traditional format with horizontal lines and vertical columns and, therefore, need to be rearranged (Figure 4(a)). An IDL program was developed to correct for the along-track and across-track shifts. The program allows for translation of the time sequential data into a spatial domain data, while for each pixel, it registers the same radiance value at a given spatial position and therefore has the advantage of keeping the original pixel values.

4.1.2. *De-striping*

Visual inspection of the Hyperion level 1B data suggests that around 25 bands contain continuous vertical strips or intermittent stripes caused by a poorly calibrated detector in
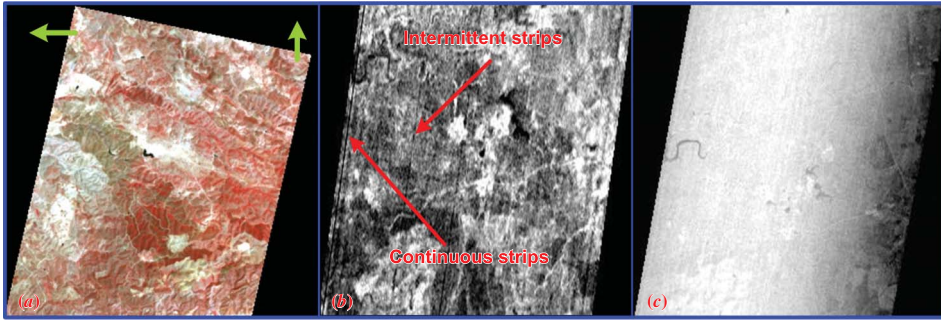
Figure 4. Different types of artefacts in the Hyperion level 1B data. (*a*) Shift in row and column which need to be corrected. The image is a colour composite from band 40 (at 752 nm), band 35 (at 702 nm), and band 30 (at 650 nm) for red, green, and blue respectively. The illustrated image was georeferenced by the image provider (USGS). (*b*) Continuous and intermittent strips, which can be found in numbers of the spectral bands, and (*c*) MNF (minimum noise fraction) band 1; the gradient change of grey tone suggests the presence of smile in the data set.

either VNIR or SWIR arrays (Han et al. 2002; Datt et al. 2003). Further analysis of the Hyperion level 1B data requires removal of the striping artefacts. The technique widely used to de-stripe the Hyperion data is based on forcing the mean and the standard deviation of each column to match the mean and standard deviation of either the corresponding band or the entire image; called local and global algorithms (Equation (2)), respectively (Datt et al. 2003). The following equations can be applied to de-stripe the EO-1 Hyperion image data (Goetz 2003):

$$X'_{ijk} = \left(X_{ijk} - \mu_{jk}\right) \frac{\sigma_k}{\sigma_{jk}} + \mu_k, \quad \text{Local algorithm,} \tag{1}$$

$$X'_{ijk} = \left(X_{ijk} - \mu_{jk}\right) \frac{\sigma_m}{\sigma_{jk}} + \mu_m, \quad \text{Global algorithm,} \tag{2}$$

where X_{ijk} is the pixel value in row i, column j, and band k; X'_{ijk} is the calculated de-striped pixel value in row i, column j, and band k; μ_k and σ_k are the mean and the standard deviation of band k; μ_{jk} and σ_{jk} are the mean and the standard deviation of column j in band k; and μ_m and σ_m are the mean and the standard deviation of the image. The detailed explanation of this approach can be found in Goetz (2003) and Datt et al. (2003). For this study, an IDL program was developed to apply the aforementioned algorithms (Equations (1) and (2)) and de-stripe the Hyperion data set.

4.1.3. Smile-effect correction

The spectral smile (frown) is a push-broom technology effect that causes a variation in central wavelength or FWHM in VNIR and SWIR bands across the width of the image array. A maximum variation of 2.7 nm has been reported for the bands in the VNIR region over the 256 pixels, while bands in the SWIR show a variation of less than 1 nm (Liao et al. 2000). This low-frequency effect of 2.7 nm variation may not affect interpretation of the Earth surface spectra since the FWHM and bandwidth are about 10 nm, but it certainly affects the highly variable and sharp 'spikes' of 0.1 nm within the atmospheric spectra and

therefore it should be removed prior to the atmospheric correction (Liao et al. 2000; Cairns et al. 2003; Datt et al. 2003).

The smile effect cannot be visualized in the individual bands, but it can be detected indirectly, e.g. using the first eigenvalue image of minimum noise fraction (MNF) space (Green et al. 1988; Goodenough et al. 2003) or measuring the spatial variation in the position of the oxygen-A absorption band near 762 nm (Green, Chrien, and Pavri 2003; Cairns et al. 2003). A brightness gradient that appears in the MNF band 1 suggests existence of the smile within the Hyperion data set. Various techniques have been developed to remove this low-frequency effect from the original Hyperion data and adjust the band centre wavelengths and bandwidth (Liao et al. 2000; Jupp et al. 2002; Feng and Xiang 2008) from which the column mean adjusted in radiance space were used in this study. By this approach, for each band, the mean value of each column is set equal to the mean value of the band assuming, on average, that the image is sufficiently homogeneous (Goodenough et al. 2003). However, the existing techniques are only able to reduce the smile effect, not to remove it completely (Jupp and Datt 2006).

4.2. Atmospheric correction

Solar radiation (emitted and scattered from the Earth surface) passes through the atmosphere before reaching a space- or airborne remote-sensing sensor, and therefore, generally, it is required for the captured data to be corrected for the effects of the atmosphere prior to quantitative analysis of surface reflectance. In past decades, several atmospheric calibration methods have been developed to remove the atmosphere effects from imagery and to retrieve surface reflectance spectra from measured radiances. The latest developments provide more accurate results by including water vapour and aerosol models in the atmospheric correction calculation (Cairns et al. 2003). Atmospheric Correction Now (ACORN), Atmospheric Removal (ATREM), Fast Line-of-sight Atmospheric Analysis of Spectral Hypercubes (FLAASH), and High Accuracy Atmospheric Correction for Hyperspectral (HATCH) data are some of the latest developed methods that are based on Moderate Resolution Atmospheric Transmission (MODTRAN) calculation (Berk, Bernstein, and Robertson 1989; Gao, Heidebrecht, and Goetz 1996; AIG 2001; Qu, Kindel, and Goetz 2003). In this study, the method (FLAASH) developed by Spectral Science Inc. (SSI) and the Air Force Research Laboratory (AFRL) was used for retrieving spectral reflectance from EO-1 Hyperion images.

4.2.1. FLAASH method

The FLAASH algorithm is one of the latest developments for atmospheric correction of space- and airborne multispectral and hyperspectral sensors. The algorithm quantifies the effects of the atmosphere with sufficient accuracy using the MODTRAN4 radiation transfer code for modelling atmospheric propagation of solar radiation (Staenz et al. 2002). The algorithm accounts for both the radiance that is reflected from the Earth's surface that travels directly into the sensor and the radiance from the surface that is scattered by the atmosphere into the sensor. The FLAASH program uses the following equation to calculate (Vermote et al. 1994; Matthew et al. 2000) surface reflectance for each pixel:

$$L = \left(\frac{A\rho}{1 - \rho_e S}\right) + \left(\frac{B\rho_e}{1 - \rho_e S}\right) + L_a, \tag{3}$$

where L is the at-sensor radiance, ρ is the pixel surface reflectance, ρ_e is an average surface reflectance for the pixel and a surrounding region, L_a is the radiance back-scattered by the atmosphere, S is the spherical albedo of the atmosphere, and A and B are coefficients that only depend on geometric and atmospheric conditions (Adler-Golden et al. 1999; Matthew et al. 2000; Staenz et al. 2002). The unknown A, B, S, and L_a are determined from MODTRAN4 spectral radiance calculations and afterwards pixel surface reflectance is calculated in all of the sensor channels from Equation (3). Then, the approximation equation (4) is used for computing a spatially averaged radiance image, L_e, from which the spatially averaged reflectance, ρ_e, is estimated:

$$L_e \approx \left(\frac{(A + B)\, \rho_e}{1 - \rho_e S} \right) + L_a. \tag{4}$$

Detailed descriptions of FLAASH and MODTRAN can be found in Staenz et al. (2002), Matthew et al. (2000), Adler-Golden et al. (1999), Kaufmann et al. (1997), Staenz and Williams (1997), Berk et al. (1998), and Berk, Bernstein, and Robertson (1989).

4.3. Post-processing

The post-processing of the Hyperion data in this study includes removal of the negative values of the pixel digital numbers (DNs) and the noise, which were both produced as the results of the pre-processing and atmospheric calibration.

4.3.1. Removal of the negative values

The algorithms that were used for de-striping and smile-effect correction may produce negative values when the operation in the first part of Equations (1) or (2) produces negative values that are larger than the band's mean. To avoid any negative pixel values in the image, an averaging filter of 3×3 windows was used. An IDL script was developed to find pixels with values less than 0 and replace them with average values calculated from their eight surrounding pixels.

4.3.2. Spectral polishing

Hyperspectral reflectance data, after atmospheric calibration, comprise noise and artefacts due to differences between the modelled and real atmosphere conditions, and limited accuracy of the methods used for processing noise (Datt et al. 2003). As a result, the reflectance data have less accuracy compared to the actual precision of the original data. In order to reduce the spectral artefacts in atmospherically corrected hyperspectral data, post-processing methods such as linear normalization were developed (Boardman 1998). The Empirical Flat Field Optimal Reflectance Transformation (EFFORT) method available in ENVI software is a mild linear correction algorithm that was used in this study to decrease the noise level in the reflectance data set.

4.4. Image classification

In this study, two classification algorithms were used to map the mine area and spatial distribution of the minerals. In the first step, the Mahalanobis Distance algorithm is applied to differentiate between main land-cover classes in the field area. This method (1) calculates

the distance towards class means for each pixel, (2) defines the shortest Euclidian distance to a class mean, (3) and then this class name is assigned to the output pixel if no distance threshold has been specified (Richards 1999). In the area of the mine, based on aerial photointerpretation and field observation, the four main land-cover classes are rock outcrop, mine waste deposits, vegetation, and water reservoirs. The collected field data were used as a training set to supervise the Mahalanobis classifier. In the second step, the spatial variations of iron oxide and carbonate minerals within the mine area were mapped using the Spectral Feature Fitting (SFF) method. The SFF is an absorption-feature-based method that compares and matches an image spectrum to a reference (endmember) spectrum using a least-squares technique (Clark, Gallagher, and Swayze 1990; Clark and Swayze 1995). The method requires that data be reduced to reflectance and that a continuum be removed from both data sets (image and reference spectra) prior to data analysis (Clark and Roush 1984; Green and Craig 1985). The outputs of the SFF classification are scale and 'root mean square' (RMS) images, which are calculated for each reference (endmember) spectrum. The scale image depicts how similar an unknown image spectrum is to the reference spectra. The pixel values close to 1 in the scale image indicate the best match to the reference material. However, the scale image may contain values larger than 1, which can be a product of selecting an incorrect wavelength range (ITT 2009). The RMS images show the root mean square error (RMSE) calculated for each reference spectrum at the pixel level, indicating the accuracy of the classified pixels (the lower the RMSE, the higher the accuracy). To improve classification accuracy in this study, the scale and RMSE image are crossed and only pixels with values close to 1 (from scale image) and pixel values close to 0 (from RMS image) are selected as the best match to the endmembers.

In this study, the endmembers were selected from the spectral library provided by USGS and the Jet Propulsion Laboratory (JPL). It is known from field measurements that the dominant iron oxide minerals in the area are identified as alunite ($KAl_3(SO_4)_2(OH)_6$), copiapite ($Fe^{2+}(Fe^{3+})_4(SO_4)_6(OH)_2 \cdot 20H_2O$), ferrihydrite (($Fe^{3+})_2O_3 \cdot 0.5H_2O$), goethite ($FeO(OH)$), haematite ($Fe_2O_3$), and jarosite ($K(Fe^{3+})_3(SO_4)_2(OH)_6$), while the dominant carbonate minerals in the area are identified as gypsum ($CaSO_4 \cdot 2H_2O$) and calcite ($CaCO_2$, $CaCO_3$). The spectral signatures of these minerals are given in Table 1.

5. Results

5.1. Pre-processing

In the first phase of pre-processing, the Hyperion images were co-aligned as described in Section 4.1. The sub-pixel shift and the spatial registration of the data were obtained by applying angular rotation in such way that for each pixel the same radiance value at a given spatial position has been registered. The developed IDL algorithm that corrects for the shifts does not apply any re-sampling techniques, and, therefore, preserves the original pixel values in the output image. Comparison of the corrected image (Figure 5(*a*)) with the uncorrected image (Figure 4(*a*)) depicts the alignment of pixels along-track and across-track. This visually can be observed, specifically for the along-track shift, by checking the stripe column in the original and corrected images. The results of the applied method compared to the counter-clockwise rotation, available in many commercial software applications, have the advantage of preserving the original pixel values.

The second phase of pre-processing concerned the removal of the vertical stripes from some of the bands in the VNIR and SWIR regions using the local method (see Section 4.1). The results suggest that the de-striping algorithm (local method), in general, works well, except for the very noisy bands (Figure 5(*b*)). The results of the local method (Equation (1),

Table 1. The dominant minerals in the field area and their diagnostic absorption bands position in VNIR–SWIR wavelength range.

Mineral type	Formula	VNIR–SWIR absorption band positions (nm)	Absorption band positions used in this study (nm)
Alunite	$KAl_3(SO_4)_2(OH)_6$	1010, 1270, 1350, 1450, 1775, 2000, 2170, 2330, 2500*	963–1033 (1003), 1235–1296 (1270), 1740–1790 (1769), 2133–2194 (2170)
Copiapite	$Fe^{2+}(Fe^{3+})_4(SO_4)_6(OH)_2 \cdot 20H_2O$	431, 468, 544, 670, 864, 1447, 1936†	772–953 (864)
Ferrihydrite	$(Fe^{3+})_2O_3 \cdot 0.5H_2O$	604, 778, 978, 1437, 1933†	824–1033 (972)
Goethite	$FeO(OH)$	494, 548, 671, 764, 963, 1451, 1935†	824–973 (922)
Haematite	Fe_2O_3	586, 663, 749, 882†	803–925(877)
Jarosite	$K(Fe^{3+})_3(SO_4)_2(OH)_6$	436, 522, 717, 924, 1466, 1848, 1933, 2264† 430, 910, 1850, 2270‡	813–993(910), 2234–2304 (2270)
Calcite	$CaCO_2, CaCO_3$	1888, 2000, 21600, 2350, 2550§ 1225, 1479, 1978, 2113, 2356	1975–2012 (1991), 2305–2355 (2335)
Gypsum	$CaSO_4 \cdot 2H_2O$	1000, 1200, between 1450–1550, 1750, 1900, between 2200–2270*	943–1044 (994), 1165–1245 (1194), 2183–2234 (2213), 2244–2284 (2270)

Note: *Hunt, Salisbury, and Lenhoff (1971).
†Crowley et al. (2003).
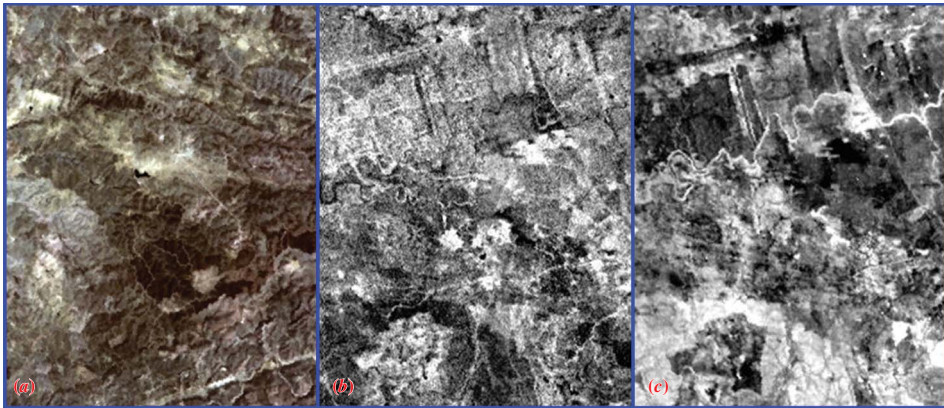‡Bishop and Murad (2005).
§Hunt and Salisbury (1971).

Figure 5. (*a*) Hyperion image after being corrected for the angular shift, (*b*) band 8 (472 nm) of the data set after removal of the stripes, (*c*) MNF band 1 calculated from the Hyperion image after being corrected for the smile/frown effects. The illustrated Hyperion image (*a*) is a colour composite of band 28 (at 701 nm), band 25 (at 671 nm), and band 18 (at 599 nm) for red, green, and blue, respectively.

Table 2. Basic statistics calculated from the bands de-striped by global and local algorithms.

Band no.	Wavelength (nm)	Minimum		Maximum		Mean		SD		PNV	
		GT	LT	GT	LT	GT	LT	GT	LT	GT	LT
2	436	−2903	1880	12529	4196	1429.5	2530.5	1242.3	186.4	9697	0
51	932	−6073	−247	8264	2634	1429.5	1260.3	1242.3	249.8	8601	2
70	1124	−6624	−103	7560	720	1429.5	364.2	1242.3	72.2	8282	22
104	1467	−5398	−67	6925	389	1429.5	184.9	1242.3	46.1	10486	47
154	1971	−5543	−66	6711	410	1429.5	204.7	1242.3	48.4	10778	40
193	2365	−4494	−25	8430	339	1429.5	141.4	1242.3	35.1	10013	17

Notes: The image bands consist of 251 columns and 300 rows with a total number of 75,300 pixels.
SD = standard deviation, GT = global algorithm, LT = local algorithm, and PNV = number of pixels with negative values in the de-striped bands.

Section 4.1) compared to the global approach show lower standard deviation and a mean close to that of the original data, while the global technique results show a wider range and high standard deviation values for the corrected bands. The basic statistic was calculated for the de-striped bands and a few examples are shown in Table 2 in order to illustrate the differences between the results of the two de-striping techniques. The calculated statistics from the de-striped spectral bands (Table 2) suggest the presence of negative pixel values mostly in the intensively noisy bands within or near the water absorption region (SWIR). The negative values were removed using a 3×3 averaging filter described earlier (see Section 4.3). Visual comparison of the de-striped image (Figure 5(*b*)) with the uncorrected image (Figure 4(*b*)) confirmed removal of the stripe from the image; both images (Figures 4(*b*) and 5(*b*)) illustrate band 8 (at 425 nm).

The EO-1 Hyperion imagery was also corrected for smile effects using the method described in Section 4.1. The MNF band 1 calculated from the Hyperion image after being corrected (Figure 5(*c*)) suggests that this method removes the gradient grey tone (Figure 4(*c*)) caused by the smile effects.

5.2. *Atmospheric correction*

The FLAASH algorithm was used to remove the effect of the atmosphere from the EO-1 Hyperion image. The model input parameters used for atmospheric correction include the mid-latitude summer atmospheric model, the urban aerosol model, and the 2-band (T-K) aerosol retrieval model (ITT 2012). The corrected image and a few examples of pixel spectra are shown in Figure 6. The upper spectrum in Figure 6 is typical of a vegetated area, while the lower spectrum in the figure represents an area of waste deposits within the mine area. For comparison, the empirical line algorithm, available in ENVI software, together with field spectra were also used to correct the EO-1 Hyperion image for atmospheric effects. However, since the FLAASH algorithm produced a better result, further data analysis was carried out using the images that were calibrated by this method.

5.3. *Post-processing*

The EO-1 Hyperion data after being de-striped and atmospherically calibrated are post-processed in order to remove the negative pixel values and reduce the noise level which
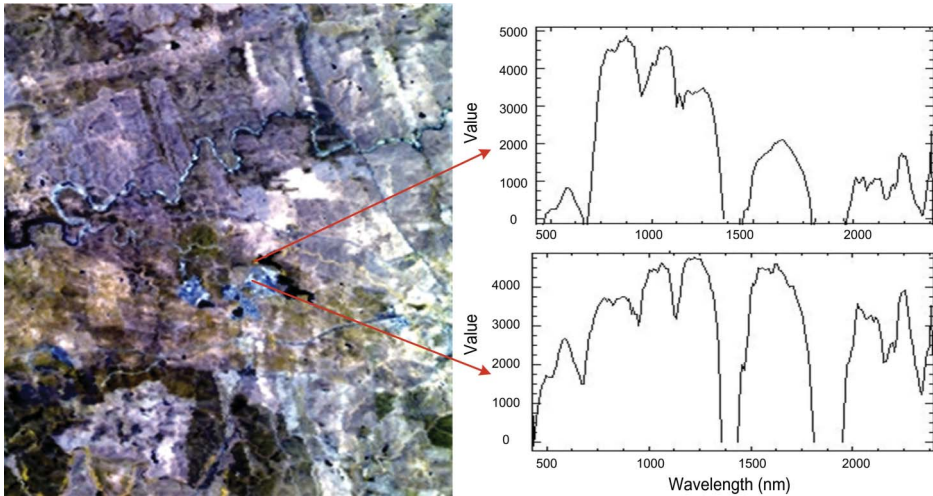
Figure 6.   The EO-1 Hyperion data after being corrected for atmospheric effects. The examples of the pixel spectra represent vegetation (upper spectrum) and mine waste deposits (lower spectrum) in the study area. The Hyperion image is a colour composite using band 43 (at 854 nm), band 33 (at 752 nm), and band 23 (at 651 nm) for red, green, and blue, respectively.

was produced as a result of pre-processing and atmospheric calibration. The negative pixel values within each band were replaced with the average value calculated from their eight surrounding pixels by applying an averaging filter of 3 × 3 windows. The mild linear correction algorithm (EFFORT) available in ENVI software was also used to reduce spectral artefacts in atmospherically corrected EO-1 Hyperion data. The image and spectra presented in Figure 6 are the final result obtained after post-processing.

5.4.   *Mapping mine waste deposits and minerals spatial variations*

The Mahalanobis Distance classification was used prior to the mineral discrimination in order to map the area of the mine where the waste rock and tailings are damped. The results illustrated successful mapping of the four main land-use classes in the field area, including the area covered by mine waste (Figure 7(*a*)). For visual comparison, a high spatial resolution photo from the same area is included (Figure 7(*b*)). Further data analysis for identification and mapping of the minerals is limited only to the area covered by the mine waste.

   The spatial variations of iron oxide and carbonate minerals within the mine area were mapped by the SFF method. The results of the SFF classification are scale and RMS images, which are calculated for each reference (endmember) spectrum. The scale images show the spatial distribution of each identified mineral, while the RMS image indicates the accuracy of the classification for each reference spectrum at pixel level. From the eight reference spectra used for classification, dominant presences of six minerals were mapped in the field area (Figure 8), while the contributions of haematite and calcite within the pixel area were not sufficient to be recognized. The basic statistic calculated from the scale and RMS images (Table 3) suggests that not all of the discriminated pixels meet the threshold as defined in Section 4.3. For example, the classified pixels in the scale images with values less than 0.8 and above 1.0 are not considered a good match and therefore need
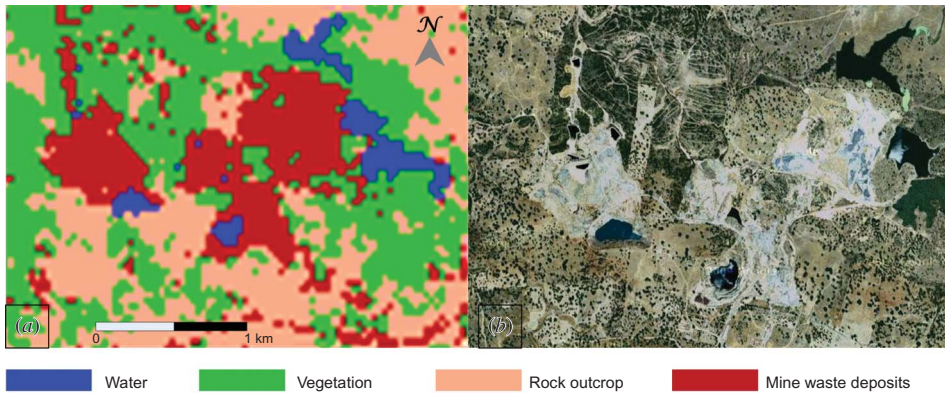
Figure 7. Classified EO-1 Hyperion image showing the main land-use classes in the field area (*a*). High spatial resolution photo from the same area for visual comparison (*b*).

to be excluded. In addition, it is also important to exclude those classified pixels with high RMSE.

In order to minimize error and to obtain a more accurate mineral mapping, from each scale image the pixels with values from 0.8 to 1.0 and from each RMS image the pixels with values lower than minimum plus 2 standard deviation were selected. The maps resulting from the selection were crossed and eventually only pixels with high match values and with low RMSE were mapped (Figure 8). The total number of pixels in each mineral class is given in Table 4. As can be seen from the table, from a total of 754 pixels that cover the test area, 43 pixels were classified as sulphide and carbonate minerals and 711 pixels showed no dominant abundance of any mineral.

5.5. *Validation of the results*

The results obtained from SFF classification were validated against field measurements. The field measurements confirm the dominant presence of the identified minerals in many
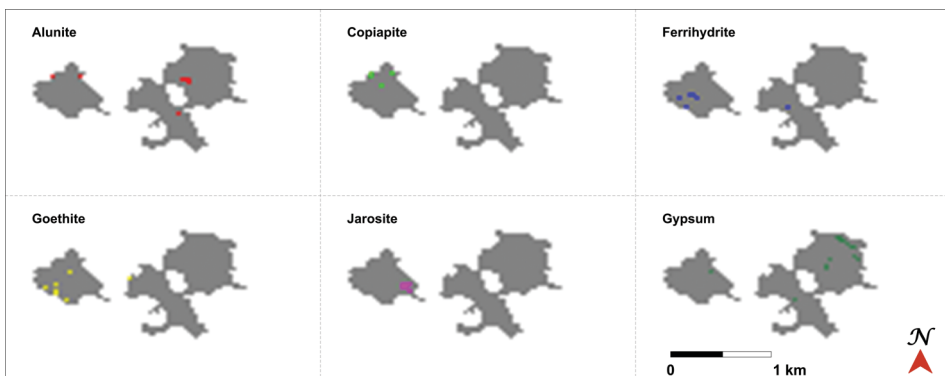

Figure 8. The images resulting from Spectral Feature Fitting method showing spatial distribution of iron oxide and carbonate minerals in the mine area. The six images were derived from crossing of the scale and RMS images. The pixels in each mineral class are those with the best match to the reference mineral and with the lowest root mean square error.

Table 3. Basic statistics calculated from the scale and RMS images.

Endmember	Scale image				RMS image			
	Min.	Max.	Mean	SD	Min.	Max.	Mean	SD
Alunite	0.5248	1.1603	0.7313	0.0903	0.1583	0.4156	0.2060	0.0227
Copiapite	0.4212	1.1687	0.5924	0.0993	0.1705	0.3794	0.2184	0.0194
Ferrihydrite	0.3428	1.2144	0.5276	0.0857	0.1856	0.3877	0.2379	0.0231
Goethite	0.3774	1.5831	0.6186	0.1292	0.1890	0.3959	0.2473	0.0241
Jarosite	0.6779	2.3685	0.9507	0.2015	0.1807	0.3769	0.2405	0.0235
Gypsum	0.6179	1.5738	0.8923	0.1335	0.1739	0.4311	0.2218	0.0215

Note: Min. = minimum, Max. = maximum, SD = standard deviation.

Table 4. Number of pixels classified within each mineral class.

Mineral class	Alunite	copiapite	Ferrihydrite	Goethite	Jarosite	Gypsum	Ferrihydrite and goethite	Classified as minerals	Classified as non-minerals
NOCP	7	4	5	6	6	14	1	43	711
Total number of pixels that cover the mine area							754		

Note: NOCP = number of classified pixels.

places within the mine area as well as within the classified pixel areas. In this study, the pixels identified as a match to reference mineral (or minerals) only suggest the abundance of the mineral or minerals within the pixel area. It should not be assumed that the entire pixel area (900 m^2) is covered by a certain mineral. It has to be emphasized that the reflectance spectra measured in the field represents an area of about 0.5 m^2, while a pixel spectrum is obtained from an area of 900 m^2 (30 × 30 m, the spatial resolution). Due to scale differences between the field measurements and image data, the calculated statistics regarding the validation of the results do not reveal the actual condition and do not show the actual differences between the SFF results and the field measurements. However, it has to be mentioned that from a total of eight endmembers identified during field measurements, two have not been detected by the SFF classifier (see Tables 1 and 4). Furthermore, the location of the field-measured spectra of different endmembers often occurs within the same pixel area, suggesting the presence of the two or three endmembers, while the results of the SFF classifier confirm the abundance of the dominant endmembers.

6. Conclusions

The results presented in this study confirm the achievement of the research objective as defined in Section 1. The method developed in this study is non-complex, simple, has undemanding capabilities in terms of field measurements, has the capability to discriminate areas covered by mine waste deposits, and provides quantitative information concerning iron oxide by-products and carbonate minerals formed at the surface. Therefore, it can be used as a preliminary application tool for monitoring the mine waste deposits.

Since the Hyperion data contain large amounts of noise and artefacts, and are affected by the atmosphere, the pre-processing and atmospheric calibrations of the data are vital and play a major role in the final output. The results suggest that the vertical stripes can be removed very well by the local algorithm except for the very noisy bands. The method developed for correcting the along-track and across-track shifts does not require re-sampling and therefore has the advantage of keeping the original pixel values.

The classification results showed that the mine waste deposits can be easily mapped using available standard algorithms. The results of mineral mapping illustrate the potential application of the EO-1 Hyperion images. However, due to the low spatial resolution of the Hyperion data (30×30 m), the results should be carefully interpreted. The field measurements confirm the dominant presence of the identified minerals within the mine area.

Acknowledgements

References

Adler-Golden, S. M., M. W. Matthew, L. S. Bernstein, R. Y. Levine, A. Berk, S. C. Richtsmeier, P. K. Acharya, G. P. Anderson, G. Felde, J. Gardner, M. Hoke, L. S. Jeong, B. Pukall, A. Ratkowski, H. H. Burke. 1999. "Atmospheric Correction for Short-Wave Spectral Imagery Based on MODTRAN4." *SPIE Proceedings on Imaging Spectrometry* 3753: 61–9.

Advanced Software Design Inc. (ASD Inc.) 2010. *FieldSpec® 3 Hi-Res Portable Spectroradiometer*. Boulder, CO: ASD, Inc. Accessed April 26, 2010. http://www.asdi.com/products/fieldspec-3-hi-res-portable-spectroradiometer.

Alastuey, A., A. García-Sánchez, F. López, and X. Querol. 1999. "Evolution of Pyrite Mud Weathering and Mobility of Heavy-Metals in the Guadiamar Valley after the Aznalcóllar Spill, South-West Spain." *The Science of the Total Environment* 242: 41–55.

Analytical Imaging and Geophysics (AIG). 2001. *ACORN User's Guide, Stand Alone Version*, 64 pp. Boulder, CO: AIG, LLC.

Barry, P. 2001. *EO-1- Hyperion Science Data User's Guide, Level 1_B*. Redondo Beach, CA: TRW, Space, Defense & Information Systems.

Berk, A., L. S. Bernstein, G. P. Anderson, P. K. Acharya, D. C. Robertson, J. H. Chetwynd, and S. M. Adler-Golden. 1998. "MODTRAN Cloud and Multiple Scattering Upgrades with Application to AVIRIS." *Remote Sensing of the Environment* 65: 367–75.

Berk, A., L. S. Bernstein, and D. C. Robertson. 1989. *MODTRAN: A Moderate Resolution Model for LOWTRAN7. GL-TR-89-0122*, 38 pp. Lincoln, MA: Air Force Geophysical Laboratory, Hanscom AFB.

Bishop, J. L., and E. Murad. 2005. "The Visible and Near Infrared Spectral Properties of Jarosite and Alunite." *American Mineralogist* 90: 1100–7.

Boardman, J. W. 1998. "Post-ATREM Polishing of AVIRIS Apparent Reflectance Data Using EFFORT: A Lesson in Accuracy Versus Precision." In *Summaries of the Seventh JPL Airborne Earth Science Workshop*, vol. 1, 53. Pasadena, CA: JPL Publication 97-2.

Buckby, T., S. Black, M. L. Coleman, and M. E. Hodson. 2003. "Fe-Sulphate-Rich Evaporative Mineral Precipitates from the Rio Tinto, Southwest Spain." *Mineralogical Magazine* 67, no. 2: 263–78.

Cairns, B., B. E. Carlson, R. Ying, A. A. Lacis, and V. Oinas. 2003. "Atmospheric Correction and Its Application to an Analysis of Hyperion Data." *IEEE Transactions on Geoscience and Remote Sensing* 41: 1232–45.

Clark, R. N., A. J. Gallagher, and G. A. Swayze. 1990. "Material Absorption Band Depth Mapping of Imaging Spectrometer Data Using a Complete Band Shape Least-Squares Fit with Library Reference Spectra." In *Proceedings of the Second Airborne Visible/Infrared Imaging Spectrometer (AVIRIS) Workshop*, 176–86. Pasadena, CA: JPL Publication 90-54.

Clark, R. N., and G. A. Swayze. 1995. "Mapping Minerals, Amorphous Materials, Environmental Materials, Vegetation, Water, Ice and Snow, and Other Materials: The USGS Tricorder Algorithm." In *Summaries of the Fifth Annual JPL Airborne Earth Science Workshop*, edited by R. O. Green, 39–40. Pasadena, CA: JPL Publication 95-1.

Clark, R. N., and T. L. Roush. 1984. "Reflectance Spectroscopy: Quantitative Analysis Techniques for Remote Sensing Applications." *Journal of Geophysical Research* 89: 6329–40.

Crowley, J. K. 1993. "Mapping Playa Evaporate Minerals with AVRIS Data: A First Report from Death Valley, California." *Remote Sensing of Environment* 44: 337–356.

Crowley, J. K., D. E. Williams, J. M. Hammarstroom, N. Piatak, I. M. Chou, and J. C. Mars. 2003. "Spectral Reflectance Properties (0.4–2.5 µm) of Secondary Fe-Oxide, Fe-Hydroxide and Fe-Hydrate Minerals Associated with Sulphide-Bearing Mine Waste." *Geochemistry: Exploration, Environment, Analysis* 3: 219–28.

Datt, B., T. R. McVicar, T. G. van Niel, D. L. B. Jupp, and J. S. Pearlman. 2003. "Preprocessing EO-1 Hyperion Hyperspectral Data to Support the Application of Agricultural Indexes." *IEEE Transactions on Geoscience and Remote Sensing* 41: 1246–59.

Doetsch, J. 1957. "Esbozo Geoquímico Y Mineralógico Del Criadero De Piritas 'Las Herrerías', Puebla De Guzmán (Huelva)." *Boletín del Instituto Geológico y Minero de Espana* 68: 225–306.

Farifteh, J., F. Van der Meer, C. Atzberger, and E. J. M. Carranza. 2007. "Quantitative Analysis of Salt-Affected Soil Reflectance Spectra: A Comparison of Two Adaptive Methods (PLSR and ANN)." *Remote Sensing of Environment* 110, no. 1: 59–78.

Feng, Y., and Y. Xiang. 2008. "Mitigation of Spectral Miss-Registration Effects in Imaging Spectrometers via Cubic Spline Interpolation." *Optics Express* 16, no. 20: 15366–74.

Folkman, M., J. S. Pearlman, L. Liao, and P. Jarecke. 2001. "EO-1 Hyperion Hyperspectral Imager Design, Development, Characterization, and Calibration. Hyperspectral Remote Sensing of the Land and Atmosphere." *Proceedings of SPIE* 4151: 40–51.

Galán, E., J. L. Gomez-Ariza, I. Gonzalez, J. C. Fernandez-Caliani, E. Morales, and I. Giraldez. 2003. "Heavy Metal Partitioning in River Sediments Severely Polluted by Acid Mine Drainage in Iberian Pyrite Belt." *Applied Geochemistry* 18: 409–21.

Gao, B. C., K. B. Heidebrecht, and A. F. H. Goetz. 1996. *Atmosphere Removal Program (ATREM) Version 2.0 Users Guide. Centre for the Study of Earth from Space/CIRES*, 26 pp. Boulder, CO: University of Colorado.

Goetz, A. F. H. 2003. EO-1 Interim Report. Accessed April 26, 2010. http://eo1.gsfc.nasa.gov/new/validationReport/Technology/JoeCD/Goetz_FinalReport.doc.

Goetz, A. F. H., G. Vane, J. Solomon, and B. N. Rock. 1985. "Imaging Spectrometry for Earth Remote Sensing." *Science* 228: 1147–53.

González, F., C. Moreno, R. Sáez, and G. Clayton. 2002. "Ore Genesis Age of the Tharsis Mining District (Iberian Pyrite Belt): A Palynological Approach." *Journal of the Geological Society* 159: 229–32.

Goodenough, D. G., A. Dyk, K. Olaf Niemann, J. S. Pearlman, H. Chen, T. Han, W. Murdoch, and C. West. 2003. "Processing Hyperion and ALI for Forest Classification." *IEEE Transaction on Geoscience and Remote Sensing* 41: 6.

Green, A. A., M. Berman, P. Switzer, and M. D. Craig. 1988. "Transformation for Ordering Multispectral Data in Terms of Image Quality with Implications for Noise Removal." *IEEE Transaction on Geoscience and Remote Sensing* 26: 65–74.

Green, A. A., and M. D. Craig. 1985. "Analysis of Aircraft Spectrometer Data with Logarithmic Residuals." In *Proceedings of the Airborne Imaging Spectrometer Data Analysis Workshop*, edited by G. Vane and A. Goetz, 111–19. Pasadena, CA: JPL Publication 86-35.

Green, R. O., T. G. Chrien, and B. Pavri. 2003. "On-Orbit Determination of the Radiometric and Spectral Calibration of Hyperion Using Ground, Atmospheric and AVIRIS under Flight Measurements." *IEEE Transaction on Geoscience and Remote Sensing* 41, no. 6: 1194–203.

Han, T., D. G. Goodenough, A. Dyk, and J. Love. 2002. "Detection and Correction of Abnormal Pixels in Hyperion Images. Geoscience and Remote Sensing Symposium, *IGARSS*." *IEEE International* 3: 1327–30.

Hudson-Edwards, K. A., M. G. Macklin, H. E. Jamieson, P. A. Brewer, T. J. Coulthard, A. J. Howard, and J. N. Turner. 2003. "The Impact of Tailings Dam Spills and Clean-up Operations on Sediment and Water Quality in River Systems: The Ríos Agrio–Guadiamar, Aznalcóllar, Spain." *Applied Geochemistry* 18, no. 2: 221–39.

Hunt, G. R., and J. W. Salisbury. 1971. "Visible and Near Infrared Spectra of Minerals and Rocks: II. Carbonates." *Modern Geology* 2: 23–30.

Hunt, G. R., J. W. Salisbury, and C. J. Lenhoff. 1971. "Visible and Near Infrared Spectra of Minerals and Rocks: IV. Sulphides and Sulphates." *Modern Geology* 3: 1–14.

ITT. 2009. *ENVI Reference Guide*. Boulder, CO: ITT Visual Information Solutions.

ITT. 2012. *ENVI Help, Standard FLAASH Input Parameters*. Boulder, CO: ITT Visual Information Solutions.

Jupp, D. L. B., and B. Datt, eds. 2006. *Evaluation of the EO-1 Hyperion Hyperspectral Instrument and Its Applications at Australian Validation Sites, 2001–2003* (2004/06), 36 pp. Canberra: CSIRO Earth Observation Centre.

Jupp, D. L. B., B. Datt, T. R. McVicar, T. G. Van Niel, J. S. Pearlman, J. Lovell, and E. G. King. 2002. "Improving the Analysis of Hyperion Red Edge Index from an Agricultural Area." In *Proceedings of SPIE Conference on Remote Sensing Asia*, Hangzhou, China.

Kaufman, Y. J., A. E. Wald, L. A. Remer, B.-C. Gao, R.-R. Li, and L. Flynn. 1997. "The MODIS 2.1-mm Channel—Correlation with Visible Reflectance for Use in Remote Sensing of Aerosol." *IEEE Transactions on Geoscience and Remote Sensing* 35, no. 5: 1286–98.

Kruse, F. A., J. W. Boardman, and J. F. Huntington. 2003. "Comparison of Airborne Hyperspectral Data and EO-1 Hyperion for Mineral Mapping." *IEEE Transactions on Geoscience and Remote Sensing* 41, no. 6: 1388–99.

Liao, L., P. Jarecke, D. Gleichauf, and T. Hedman, 2000, "Performance Characterization of the Hyperion Imaging Spectrometer Instrument." *Proceedings of SPIE* 4135: 264–275.

Matthew, M. W., S. M. Adler-Golden, A. Berk, S. C. Richtsmeier, R. Y. Levine, L. S. Bernstein, P. K. Acharya, G. P. Anderson, G. W. Felde, M. P. Hoke, A. Ratkowski, H.-H. Burke, R. D. Kaiser, D. P. Miller. 2000. "Status of Atmospheric Correction Using a MODTRAN4-based Algorithm." *SPIE Proceedings, Algorithms for Multispectral, Hyperspectral, and Ultraspectral Imagery VI* 4049: 199–207.

Pamo, E., D. Barettino, C. Antón-Pacheco, G. Ortiz, J. C. Arranz, J. C. Gumiel, B. Martinez-Pledel, M. Aparicio, and O. Montouto. 1999. "The Extent of the Aznalcollar Pyritic Sludge Spill and Its Effects on Soils." *Science of the Total Environment* 242: 57–88.

Pearlman, J. S., P. S. Barry, C. C. Segal, J. Shepanski, D. Beiso, and S. L. Carman. 2003. "Hyperion, a Space-Based Imaging Spectrometer." *IEEE Transactions on Geoscience and Remote Sensing* 41, no. 6: 1160–73.

Pinedo Vara, I. 1963. *Piritas de Huelva. Su historia, minería y aprovechamiento*, 1003 pp. Madrid: Summa.

Qu, Z., B. C. Kindel, and A. F. H. Goetz. 2003. "The High Accuracy Atmospheric Correction for Hyperspectral Data (HATCH) Model." *IEEE Transactions on Geoscience and Remote Sensing* 41: 1223–31.

Richards, J. A. 1999. *Remote Sensing Digital Image Analysis*, 240 pp. Berlin: Springer-Verlag.

Sáez, R., C. Moreno, and F. González. 2008. "Synchronous Deposition of Massive Sulphide Deposits in the Iberian Pyrite Belt: New Data from Las Herrerías and La Torerera Ore-Bodies." *Comptes Rendus Geosciences* 340, no. 12: 829–39.

Staenz, K., R. A. Neville, S. Clavette, R. Landry, and H. P. White. 2002. "Retrieval of Surface Reflectance from Hyperion Radiance Data." *IEEE Geoscience and Remote Sensing Letters* 1, no. 2: 1419–21.

Staenz, K., and D. J. Williams. 1997. "Retrieval of Surface Reflectance from Hyperspectral Data Using a Look-up Table Approach." *Canadian Journal of Remote Sensing* 23, no. 4: 354–68.

Swayze, G. A., K. S. Smith, R. N. Clark, S. J. Sutley, R. M. Pearson, J. S. Vance, P. L. Hageman, P. H. Briggs, A. L. Meier, M. J. Singleton, S. Roth. 2000. "Using Imaging Spectroscopy to Map Mine Sites." *Environmental Science and Technology* 34: 47–54.

Velasco, F., A. Alvaro, S. Suarez, J. M. Herrero, and I. Yusta. 2005. "Mapping Fe-Bearing Hydrated Sulphate Minerals with Short Wave Infrared (SWIR) Spectral Analysis at San Miguel Mine Environment, Iberian Pyrite Belt (SW Spain)." *Journal of Geochemical Exploration* 87, no. 2: 45–72.

Vermote, E. F., D. Tanre, J. L. Deuze, M. Herman, and J. J. Morcrette. 1994. *Second Simulation of the Satellite Signal in the Solar Spectrum (6s). 6s User Guide Version 6.0*, 134. Greenbelt, MD: NASA-GSFC.

White, H. P., K. S. Khurshid, R. Hitchcock, R. Neville, L. Sun, C. M. Champagne, and K. Staenz. 2004. "From At-Sensor Observations to At-Surface Reflectance-Calibration Steps for Earth Observations Hyperspectral Sensors." In *IGARSS'04, Proceedings of the IEEE International Geoscience and Remote Sensing Symposium*, Anchorage, Alaska, vol. 5, 3241–4.